Role of composition in fracture behavior of two-phase solids

Subrat Senapati,[1,*] Anuradha Banerjee,[1,†] and R. Rajesh[2,3,‡]
[1]*Department of Applied Mechanics, IIT Madras, Chennai 600036, India*
[2]*Institute of Mathematical Sciences, C.I.T. Campus, Taramani, Chennai 600113, India*
[3]*Homi Bhabha National Institute, Training School Complex, Anushakti Nagar, Mumbai 400094, India*

(Received 20 October 2022; accepted 11 April 2023; published 3 May 2023)

In a two-phase solid, we examine the growth of a preexisting macroscopic crack based on simulations of a random spring network model. We find that the enhancement in toughness, as well as strength, is strongly dependent on the ratio of elastic moduli as well as on the relative proportion of the phases. We find that the mechanism that leads to enhancement in toughness is not the same as that for enhancement in strength; however, the overall enhancement is similar in mode I and mixed-mode loading. Based on the crack paths, and the spread of the fracture process zone, we identify the type of fracture to transition from nucleation type, for close to single-phase compositions, whether hard or soft, to avalanche type for more mixed compositions. We also show that the associated avalanche distributions exhibit power-law statistics with different exponents for each phase. The significance of variations in the avalanche exponents with the relative proportion of phases and possible connections to the fracture types are discussed in detail.

DOI: 10.1103/PhysRevE.107.055002

I. INTRODUCTION

Biological materials such as wood, bone, and nacre are inherently multiphased in their constitution. In such natural materials, even with the same constituents, by controlling the relative proportion of the phases and their spatial arrangements, a wide range of effective mechanical and fracture properties can be achieved [1–5]. For man-made materials also, with advancements in manufacturing technologies, it is possible to control and fine tune the composition, even at the microscopic scale [6,7]. There is continuing effort towards development of novel multiphase materials that can be used in engineering applications and determination of optimum combinations of phases as well as development of better manufacturing techniques that induce minimal undesirable side effects [8–10]. For reliable use, as well as optimum design of man-made multiphase solids, developing insights by modeling their fracture behavior assumes paramount significance.

One of the biggest advantages of multiphase materials is the enhancement of effective fracture resistance in comparison to that of their constituent phases. Even with inherently brittle constituents, it is possible to achieve stable propagation of damage, prior to final failure [11,12]. In addition, fracture paths can often be controlled by arranging compliant inclusions in the path of a propagating crack, thereby increasing the resistance to crack growth [11]. Further increase in performance can be obtained by spatial patterning. In some natural materials like nacre, deep sea sponge, and bone the multiphase constituents are distributed in specific spatial patterns. In artificial multiphase material created through 3D printing, it has been shown that specific morphological arrangement of hard and soft phases leads to superior mechanical and fracture properties compared to their constituents [12,13]. However, design and development of these material systems require understanding of the role of composition on all the other performance indices as well, such as strength, stiffness, and damage nucleation and growth. These indices, in addition to the percentage of each phase, also strongly depend on the comparative elastic and fracture properties of the individual phases [14,15].

Damage in heterogeneous or multiphase materials, typically in the form of microcracks, nucleates at multiple independent sites. Further microcracking occurs not only in the neighborhood of these microcracks but also at other locations in the domain even without any stress concentrators. These microcracking events typically occur intermittently and are known to release elastic stress waves referred to as acoustic emission (AE) activity. Clusters or avalanches of AE signals are recorded as damage grows until catastrophic failure. The distribution of the cluster or avalanche sizes, energy, duration, and waiting time between two successive events has been shown for several heterogeneous materials to exhibit power-law behavior that spans several decades [16–19].

Classical fracture theory-based failure criteria have limited capability in predicting fracture in heterogeneous materials due to subcritical nucleation and growth of interacting multiple microcracks. Among the various numerical techniques that have been used to simulate fracture processes in heterogeneous materials, discrete lattice-based models have found wide popularity [20,21]. These models have been shown to be effective in reproducing several features of experimental fracture data of heterogeneous media, such as power-law statics of cracking events [22–25], quasibrittle macroscopic response

*subrat.senapati52@gmail.com
†anuban@iitm.ac.in
‡rrajesh@imsc.res.in

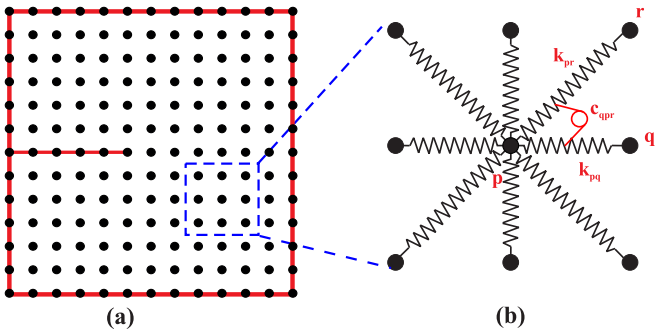

FIG. 1. Discretization of a continuum domain into a spring network.

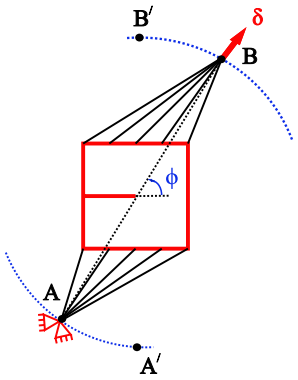

FIG. 2. Fixture for simulating mixed-mode fracture.

resulting from inherent disorder [26,27], prepeak and post-peak response [28–32], complex failure paths [16,31,33], etc. Additionally, from the simulations it is possible to gain insights into the mechanisms that lead to enhancement of toughness, such as formation of large process zones, increased delocalization of singular stresses, crack path deflection, etc. [34–37]. The factors that control these mechanisms have been identified to be relative proportion of phases, elastic ratio between the phases [38,39], spatial patterns [36], differences in fracture characteristics of the phases [21], hierarchical architecture of phases [33], etc. While the primary focus of studies on the effect of heterogeneity on fracture have focused on mode I crack growth, various aspects of crack growth under more realistic mixed-mode conditions have also garnered interest, such as determining failure criteria based on mode I fracture parameters [40], finding the effect of elastic modulus ratio on global fracture parameter (stress intensity factor) expressions as well as crack paths [38], finding the effect of elastic and local fracture characteristics in simulation of continued stable crack growth in a composite laminate [21], etc.

The type of fracture, based on simulations of a lattice-based random fuse network model, has been shown to be of three types: nucleation, avalanche, or percolation type. For a given sample size, the avalanche-type fracture transitions to nucleation type for small disorder and to percolation for the limit of large disorder [22]. Similar transitions can be driven by the variations in the hardening behavior of a quasibrittle solid [23]. In these studies the system was taken to be elastically homogeneous, and the disorder was only in the fracture characteristics.

In the fracture of multiphase solids, is the observed enhancement in mode I toughness strongly dependent on the ratio of elastic moduli? Do the mechanisms that operate in mode I also occur in mixed mode, and is the enhancement similar? How are the avalanche statistics different from a single-phase disordered solid? And is there any transition between the fracture types at different compositions? In the present work, using a random spring network model we simulate the growth of a preexisting macroscopic crack in a two-phase solid. The elastic behavior of springs is taken to be either a hard phase or a compliant soft phase, with the hard phase being the less dissipative one. We find the enhancement in toughness as well as strength to be strongly dependent on the elastic moduli as well as on the relative proportion of the phases. We find that the mechanism that leads to enhancement in toughness is not the same as that for enhancement in strength; however, the overall enhancement is similar in mode I and mixed-mode loading. We also develop a discussion of the type of fracture based on the crack paths and the spread of the fracture process zone. We show that the associated avalanche distributions exhibit power-law statistics with different exponents for each phase. The significance of variations in the avalanche exponents with the relative proportion of phases and possible connections to the fracture types are discussed in detail.

II. MODEL

Domain discretization

A rectangular domain representing a solid with a macroscopic edge crack is discretized using a 100×100 square lattice of lattice spacing a_0, as shown in Fig. 1(a). Each lattice site (p) is connected with its nearest (q) and next nearest neighbors (r) with extensional springs of spring constants k_{pq} and k_{pr} respectively, while every triad of sites $\langle qpr \rangle$ is connected with a rotational spring of spring constant c_{qpr}, as shown in Fig. 1(b).

To simulate mixed-mode loading, the lattice sites at the top edge are connected to a loading pin through struts and those at the bottom edge to a fixed pin, as shown in Fig. 2. The angle between the loading axis and the initial crack plane is denoted by ϕ. Thus, for $\phi = 90^\circ$, crack growth occurs in opening mode (mode I), while for $\phi = 45^\circ$, crack growth occurs in mixed mode.

The elastic behavior of the springs is determined based on the continuum properties of the representative solid [41,42]. The relation between the continuum and the spring network is established through the equivalence of their stored energy densities. The spring network has both extensional and rotational springs, hence the potential energy Φ has an extensional component Φ_{ext} and a rotational component Φ_{rot}:

$$\Phi = \Phi_{\text{ext}} + \Phi_{\text{rot}}. \tag{1}$$

The net extensional potential energy of the system is

$$\Phi_{\text{ext}} = \sum_{\langle ij \rangle} \frac{1}{2} k_{ij} (|\vec{r}_i - \vec{r}_j| - a_{ij})^2, \tag{2}$$

where k_{ij} is the stiffness of spring connecting lattice points i and its neighbor j and the sum is over all pairs of sites

connected by extensional springs including nearest and next-nearest pairs. a_{ij} denotes the undeformed distance between points i and j, and $\vec{r}_i$ and $\vec{r}_j$ are their respective position vectors. Similarly, the rotational potential energy component of the system is calculated as

$$\Phi_{\text{rot}} = \sum_{\langle pqr \rangle} \frac{1}{2} c_{pqr} \left(\theta_{pqr} - \frac{\pi}{4}\right)^2, \tag{3}$$

where c_{pqr} represents the rotational stiffness of the spring connecting the triad of sites $\langle pqr \rangle$ [see Fig. 1(b)] and the summation $\langle pqr \rangle$ is over all possible triads. In the undeformed lattice configuration $\theta_{pqr} = \frac{\pi}{4}$ [Fig. 1(b)]. The potential energy Φ in Eq. (1) per unit volume is equated with the strain energy density of the continuum to express the elastic parameters Young's modulus E and Poisson's ratio ν in terms of lattice parameters. For a homogeneous isotropic system, it can be shown that [41]

$$E = \frac{8k\left(k + \frac{c}{a_0^2}\right)}{3k + \frac{c}{a_0^2}}, \tag{4}$$

$$\nu = \frac{\left(k - \frac{c}{a_0^2}\right)}{3k + \frac{c}{a_0^2}}, \tag{5}$$

where $2k$ is the spring constant of nearest-neighbor springs, k is the spring constant of the next-nearest neighbor springs, $c_{pqr} = c$, and $a_0 = 0.5$ mm is the undeformed distance between nearest-neighbor sites.

We now explain how the two-phase solid is modeled using the spring network model. To model a two-phase material that is obtained by randomly mixing hard and soft phases, each lattice site is first assigned to be either soft or hard. We denote the fraction of sites that are soft by r. Thus $r = 0$ and $r = 1$ correspond to homogeneous hard and soft phases, respectively. We fix the elastic modulus of the hard phase to be $E_h = 200$ GPa. The elastic modulus of the soft material E_s is chosen to be $E_s = E_h/\alpha$, where $\alpha > 1$. The Poisson's ratio is chosen to be same for both, $\nu = 0.3$. The choice of the magnitude of the parameters falls in the ranges of ceramic matrix composites and metal-ceramic composites. To assign the spring constants, we proceed as follows. First, we determine values of the spring constants for a homogeneous system of either only soft bonds or only hard bonds. Then, for each lattice site, the springs connecting it to the sites in the south, southwest, west, and northwest are assigned according to the elastic properties of that site. The spring constants of all eight rotational springs associated with the site are assigned according to the elastic properties of the site. This ensures a unique assignment of spring constants, once the hard and soft phases are distributed [41].

To simulate fracture, we impose a criterion for a spring to break. We adopt a common stress threshold for all bonds, irrespective of whether it is soft or hard. This will correspond to different strain thresholds for the soft and hard bonds. In the absence of any disorder, the anisotropy of the lattice plays a role in mixed-mode fracture [43]. This issue is resolved in the presence of a small amount of disorder, which is introduced by choosing the threshold values for stress from a normal distribution of mean 2.5 kN/mm^2 and standard deviation equaling 4% of the mean. A spring breaks when its length increases beyond a threshold. The rotational bonds associated with a broken bond are also considered to be broken.

For fracture analysis, an edge crack of size 30 mm is inserted exactly at the midpoint of the y plane by removing bonds common to the 50th and 51st rows of the network, as shown in Fig. 1(a).

To study the effect of heterogeneity, we have considered $r = [0.1, 0.2, 0.3, 0.4, 0.5, 0.6, 0.7, 0.8, 0.9]$, and to see the effect of elastic modulus ratio α, we have studied three values of $\alpha = 20$, 10, and 5. In systems having different α values, the $E_h = 200$ GPa is fixed, and the corresponding E_s are calculated using respective α. For every system having a unique combination of α and r, 20 realizations are simulated for fracture related studies and 60 realizations for avalanche studies. This ensures that the results are not sensitive to a particular choice of spatial assignment of hard and soft phases.

The system is loaded by displacing the loading pin quasi statically at 0.01 mm per loading step. In the choice of step size, we have checked for the independence of the avalanche statistics and macroscopic response on the step size by simulating with half the step size as well as double the step size (for select parameters) with no change in exponents or overall response. The applied displacement is transmitted to the network through stiff trusses as shown in Fig. 2. The displacement components of the lattice point p are converted into respective force components using Newton's law of motion. An extra dissipative force term is added for quick equilibration of the system. The net force interaction of the lattice point with its neighbors is calculated as

$$\vec{a}_p = -\nabla_{\vec{r}_p} \phi, \tag{6}$$

where mass is set to unity. To attain equilibrium we introduce a dissipative force, $-\gamma \vec{v}_p$, where the damping coefficient γ is set to be 0.8. Once $\vec{a}_p$ is known, the corresponding position vector at time $t + \Delta t$ is calculated in terms of the position vector of the last two time steps, $\vec{r}_p(t)$ and $\vec{r}_p(t - \Delta t)$, using the Verlet algorithm as

$$\vec{r}_p(t + \Delta t) = \vec{r}_p(t)(2 - \gamma \Delta t) - \vec{r}_p(t - \Delta t)(1 - \gamma \Delta t) + \vec{a}_p(\Delta t)^2. \tag{7}$$

In the derivation for the dissipative term, the velocity is evaluated by the backward difference formulas $\vec{v}_p(t) = [r(t) - r(t - \Delta t)]/\Delta t + O(\Delta t)$. The position vector $\vec{r}_p$ is calculated iteratively using Eq. (7) till the system reaches static equilibrium. Static equilibrium is assumed to be reached when the kinetic energy of each particle is lower than a predefined threshold. We further check that the total forces in the top and bottom loading pins are equal. After equilibration, the springs are checked for breakage, the system is reequilibrated, and the steps are repeated until no further breakage occurs within the increment.

III. RESULTS

A. Mechanical properties

We first determine the effect of the relative composition of the two phases on the effective macroscopic response. Simulations of deformation and fracture of the rectangular domain with a preexisting edge crack, of size 0.6 times the width, were performed by applying the displacement load at

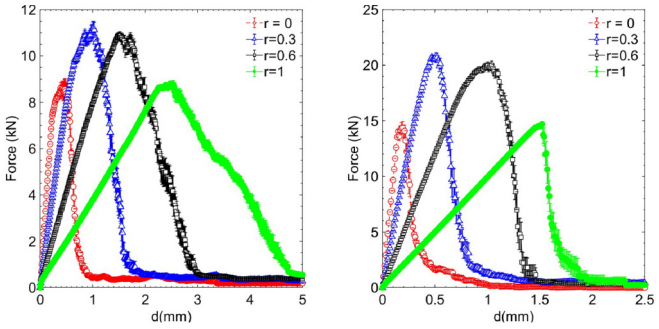

FIG. 3. Averaged force-deflection curve for $\alpha = 10$, and different r for (a) mode I and (b) mixed mode.

the loading pin incrementally, and the corresponding reaction forces at the loading pin were calculated in the direction of applied displacement. Figure 3(a) shows the macroscopic response for mode I loading, obtained for a range of compositions, r, with fixed $\alpha = 10$, and each data point is averaged over 20 realizations. For both single phases ($r = 0$ and 1), the response is nearly linear up to the peak load, and upon further extension, the resulting response shows a sharp decline in the load-bearing capacity. For two-phase composition ($0 < r < 1$), however, after the initial linear elastic response, there is nonlinearity prior to the peak load. This is a consequence of springs breaking at multiple locations. Compared to the overall response of the homogeneous phase, there are enhancements in strength as well as energy dissipated during the crack growth until complete failure.

The macroscopic response to mixed-mode loading, presented in Fig. 3(b), has similar features to that for mode I loading, in terms of the initial linear response followed by nonlinearity prior to peak load. The load drop, however, is significantly more gradual than mode I for higher r. The enhancement in strength with r shows a similar trend as seen in mode I.

To establish the effect of α, the ratio between the elastic moduli of the two phases, on the extent of enhancement of strength, similar sets of analyses were performed keeping $E_h = 200$ GPa for $\alpha = 5$ and 20 also. In Figs. 4(a) and 4(b), the strengths are normalized by the strength at $r = 0$. As evident in Fig. 4(a), for mode I the normalized strength has an optimum range for r between 0.1 and 0.6, for which the strength is near its highest. Moreover, at least 20% increment in strength is observed for all α in the range of $r = [0.1–0.7]$. For mode I, there is utmost a weak dependency of the gain in strength on α (at $\alpha = 20$, the enhancement is somewhat reduced due to edge effects as many broken springs are close to the upper and lower edges). Comparatively, in mixed-mode loading, the enhancement in strength [Fig. 4(b)] is more sensitive to the ratio α than in mode I. For $\alpha = 5$, in the range of $r = 0.1–0.8$ the strength enhancement is between 10%–15%, whereas for mode I it was 20%–40%. For higher α, in contrast, the enhancement is comparable to mode I, and for $r = 0.2–0.5$, is higher in mixed mode than seen in mode I.

The effect of α on the total energy supplied (EnS) or toughness, which is the area under the force-deflection curve,

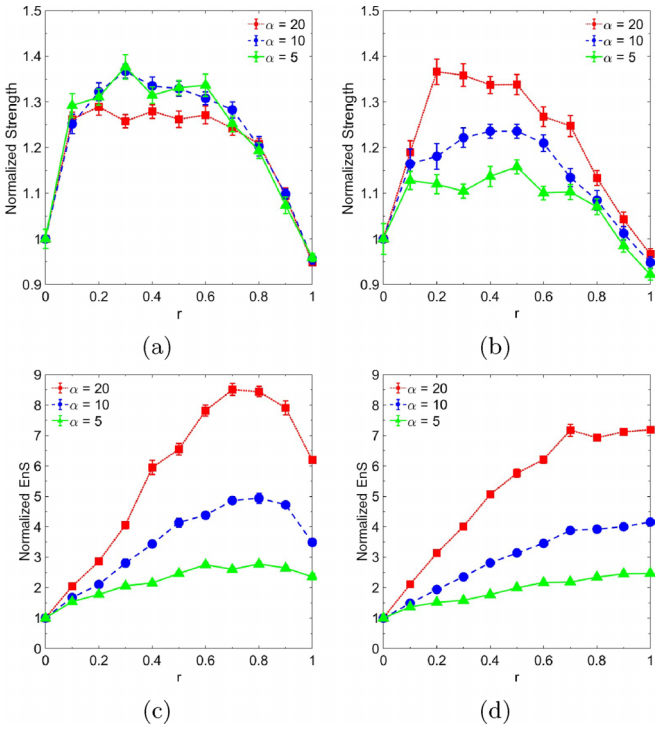

FIG. 4. Effect of r and α on normalized strength for (a) mode I and (b) mixed mode, and on normalized energy supplied (EnS) for (c) mode I and (d) mixed mode.

is shown in Figs. 4(c) and 4(d). EnS is dependent on both effective stiffness and the fracture events happening during loading. EnS has two contributions. The first is from the initial portion of the force-deflection curve where there are very few fracture events and the contribution to EnS is strongly dependent on the effective compliance of the system. The second part is from the later portion of the force-deflection curve and the contribution to EnS is determined by fracture events. Figure 4(c) for mode I fracture shows that a less compliant sample can have a larger EnS, as is clear from the behavior close to $r = 1$. However, for mixed-mode loading, this feature is absent, as can be seen from Fig. 4(d). Also, it is seen in Fig. 4(c) that in mode I fracture the enhancement in EnS is significant for higher fractions of softer phase ($r > 0.5$). It is interesting to note that while the modulus ratio has a strong effect on the enhancement in total energy supplied, the effect on strength is comparatively insignificant. In contrast to mode I, in mixed mode the enhancement in the energy supplied for failure is seen to increase with r till it saturates beyond $r = 0.7$ as shown in Fig. 4(d). The optimum seen in mode I normalized EnS is absent for mixed mode.

B. Microscopic details of fracture process

To gain an insight into the mechanisms of observed enhancement of both strength and toughness, as well as increase of quasibritility with heterogeneity, we now study the microscopic details of the fracture process such as the extent of damage and statistics of broken bonds of different phases.

First, to understand the enhancement in strength, we examine the damage patterns at peak load of a single realization,

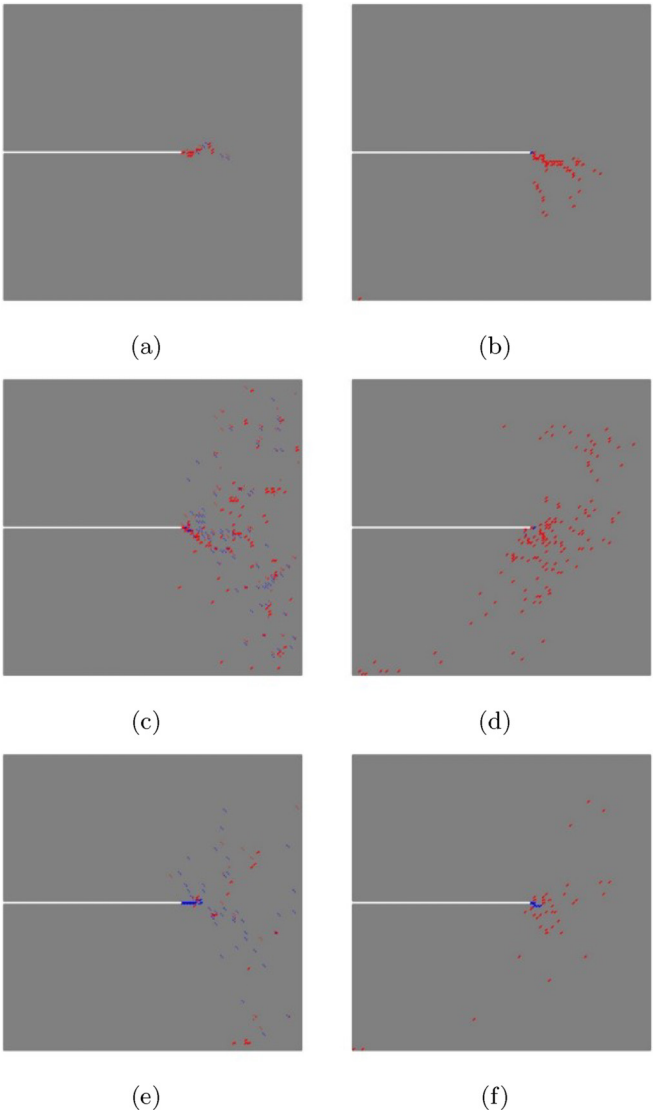

FIG. 5. Failure path at peak load of a single realization for mode I with (a) $r = 0.2$, (c) $r = 0.5$, and (e) $r = 0.8$ and for mixed mode with (b) $r = 0.2$, (d) $r = 0.5$, and (f) $r = 0.8$. Gray corresponds to unbroken bonds, blue to broken soft bonds, and red to broken hard bonds.

as shown in Fig. 5, where unbroken bonds are gray, broken soft bonds are blue, and broken hard bonds are red. When the domain is predominantly hard phase ($r = 0.2$), as in Fig. 5(a) for mode I, the damage is localized in the hard phase ahead of the crack tip and appears as contiguous clusters in red aligned to the initial crack plane. There is no noticeable breakage in the soft phase. Similarly, for $r = 0.8$ in Fig. 5(e), which is predominantly soft phase, the cluster (blue) formation is now in soft phase and is aligned with the initial crack plane with marginal damage in hard phase.

For the evenly mixed composition at $r = 0.5$, which belongs to the range of compositions in which considerable enhancement of strength is seen for all α, there is significant damage nucleation ahead of the crack tip in the hard phase, appearing as neighboring clusters in red, in contrast to $r = 0.2, 0.8$, which deviates from the initial crack plane [see

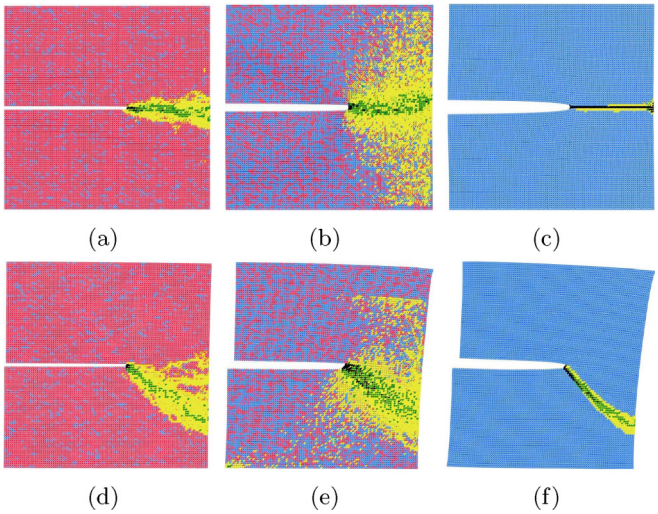

FIG. 6. Contours of failure paths averaged over 20 realizations for $\alpha = 20$ under mode I loading with (a) $r = 0.1$, (b) $r = 0.6$, and (c) $r = 1.0$ and under mixed-mode loading with (d) $r = 0.1$, (e) $r = 0.6$, and (f) $r = 1.0$. Bonds that have probability of failure in the ranges 0%–25%, 25%–50%, and greater than 50% are colored yellow, green, and black, respectively. The bonds that are not broken in any of the realizations are colored red (hard) and blue (soft), based on the composition of a single realization.

Fig. 5(c)]. There is also diffused damage growth in the hard phase farther from the crack tip. In the soft phase, however, the cluster formation is marginal except very near the crack tip as a connection between two red clusters. The correlation of the damage pattern at $r = 0.5$ with enhancement in strength suggests the mechanism of strength enhancement to be due to (1) localized damage growth in hard phase as growing clusters ahead of crack tip that are not aligned with the initial crack plane and (2) the higher resistance (dissipation energy) of the softer phase, which disallows coalescence of red clusters of broken hard phase up to peak load before formation of the eventually connected crack path. As a consequence, the resulting crack paths are expected to be more tortuous at $r = 0.5$. Damage growth patterns in mixed mode have similar mechanisms as in mode I, as seen in Figs. 5(b), 5(d), and 5(f), with the damage oriented asymmetrically at an angle to the initial crack plane consistent with the mixed-mode nature of applied load.

To further illustrate the effect of heterogeneity on the spread of the fracture process zone we show the spatial location of broken bonds as contour plots, constructed from 20 realizations, in Fig. 6. There are some bonds that are not broken in any of the 20 realizations. To make the visualization of the composition into hard and soft phases clearer, we have colored the unbroken bonds as red (hard) and blue (soft) based on the composition of a single realization. The bonds that have probability of failure in the ranges 0%–25%, 25%–50%, and greater than 50% are colored yellow, green, and black, respectively. Note that we cannot further distinguish these broken bonds into soft or hard phases because they may not be the same in the different realizations. We first discuss mode I loading. As seen from Figs. 6(a)–6(c), the probability of breaking bonds in the initial crack plane remains higher even in the

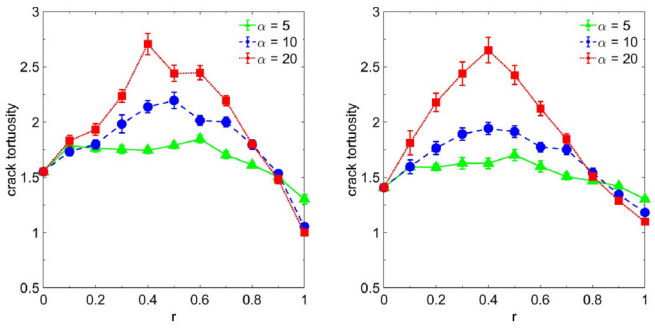

FIG. 7. Effect of r and α on crack tortuosity for (a) mode I loading and (b) mixed-mode loading.

presence of heterogeneity. The breaking of bonds in the region above and below the crack plane is indicative of tortuous crack growth. The bigger the size of the process zone, the more tortuous the crack path. For heterogeneous systems ($r \neq 0, 1$), from Fig. 6, it can be seen that the tortuosity increases from $r = 0.1$ to $r = 0.6$, and subsequently reduces with further increase in r. For a given r, the process zone size increases with α as seen by comparing the process zones in Fig. 6 for $\alpha = 20$ with the process zones for $\alpha = 10$, shown in Fig. 15 in the Appendix. However, when the system is homogeneous ($r = 1$), the crack grows mostly along its initial plane, as seen in Fig. 6(c). It is evident that at higher heterogeneity (high α and r in the range 0.3–0.7), the growth of damage is significantly more diffused, and the crack path is not as well defined as in case of homogeneous composition ($r = 0$ and 1). For mixed-mode loading, the observed crack paths, presented in Figs. 6(d)–6(f), show effects of mode mixity as the crack paths are inclined to the initial plane of macroscopic crack. The effect of increasing α resulting in a larger process zone size is also seen in the growth of the crack under mixed-mode conditions (see Fig. 15 in the Appendix). For a strongly heterogeneous system (higher α and $r = 0.3$–0.6), in addition to the process zone around the crack path, bonds near the loading pin also break. This is because in mixed-mode loading the loads are more concentrated on the truss members closer to the top-right and bottom-left corners [see Fig. 6(e)], resulting in local bond breakages.

We now quantify the tortuosity of the fracture path by defining crack tortuosity to be the ratio of the overall crack length to the distance between the endpoints of the crack. The average crack tortuosity for both mode I and mixed mode, shown in Figs. 7(a) and 7(b), is seen to be high in the range of composition, consistent with the enhancement in strength seen in Figs. 4(a) and 4(b).

In the strength enhancement, shown earlier in Fig. 4(a), only a weak dependency on α was observed in mode I. This could be a result of the opposing effects of higher α on strength: (1) enhancement due to the higher resistance of the softer phase which results in higher tortuosity and (2) reduction of strength due to both the system having lower initial stiffness as well as higher reduction in stiffness (from initial to the instant at peak load) due to the larger number of bonds that break up to peak load for higher α, both locally ahead of the crack tip as well as in the diffused manner farther away, leading to nonlinearity in the macroscopic response. Therefore, while higher α encourages more tortuosity in the path (see Fig. 7), thereby enhancing the strength, it also results in a more compliant system, resulting in lower buildup of stresses for the same applied strains, thus, nullifying the enhancement effect across α in mode I. In the mixed-mode case the effect of enhancement dominates, while the difference in tortuosity is significantly higher at $\alpha = 20$, 1.5 times that at $\alpha = 5$, whereas, in mode I, the tortuosity at $\alpha = 20$ is 1.3 times that of at $\alpha = 5$, the corresponding differences between $\alpha = 5$ and 20 in the initial stiffness, and the change in stiffness up to peak load is comparable to within 2% between the modes. This inference is consistent with the significant role of α on the enhancement of strength observed earlier for mixed-mode loading in Fig. 4(b).

To quantify the extent of damage about the mean direction of crack growth, we show the comparative angular distribution of the number of broken soft and hard bonds (normalized with the maximum for clarity) in Fig. 8. It is clear that the hard bonds tend to break for a wider range of angles for higher r. The softer bonds, however, irrespective of the composition, break only in a narrow band around the most likely path. For mode I, the crack grows along 0°, and for mixed mode, it grows along −30° with respect to the initial crack plane.

We now examine the role of the comparative breakage of hard and soft bonds towards the enhancement of strength and toughness. In Fig. 9(a) the number of soft springs that break until final failure show a nearly proportionate increase with r. Interestingly, the number of hard bonds that breaks prior to final separation of solid, as shown in Fig. 9(c), while initially increasing with r, reaches a maximum beyond which it decreases with increasing r. It is to be noted that if the cracks were perfectly linearly along the initial plane, then the number of broken hard bonds would have decreased linearly with r. This behavior is manifested in a decrease in the total number of bonds broken for larger r, as shown in Fig. 9(e). It is interesting to note that while the number of soft bonds that break is marginally sensitive to the ratio between the elastic modulus of the phases, for a similar increase in the modulus ratio, the number of hard bonds that break shows a significant increase. This increase of total number of broken bonds with α is consistent with the increase in process zone size with α, as seen in Figs. 6 and 15. At lower r, the total number of bonds broken, as shown in Fig. 9(e), are close to the number of hard bonds broken, but subsequently, closer to $r = 1$, the number of soft bonds broken contributes significantly to the overall count of broken bonds. This is also seen in Fig. 16(a) in the Appendix, which summarizes the percentage contribution of the two phases in the total number of broken bonds. The higher the ratio between the modulus of the two phases, the more dominant is the contribution of the breakage of hard bonds in the combined count. Similar to the fracture process as seen during mode I crack growth, in mixed mode also the breakage of hard bonds constitutes a significantly larger fraction of the total bonds that are broken [see Figs. 9(b), 9(d), 9(f), and 16(b)]. The crossover for $\alpha = 5$ occurs at $r \sim 0.7$ and for higher α shifts further closer to r=1.

Breakage of both extensional and torsional bonds releases the deformation energy stored in them. The comparative

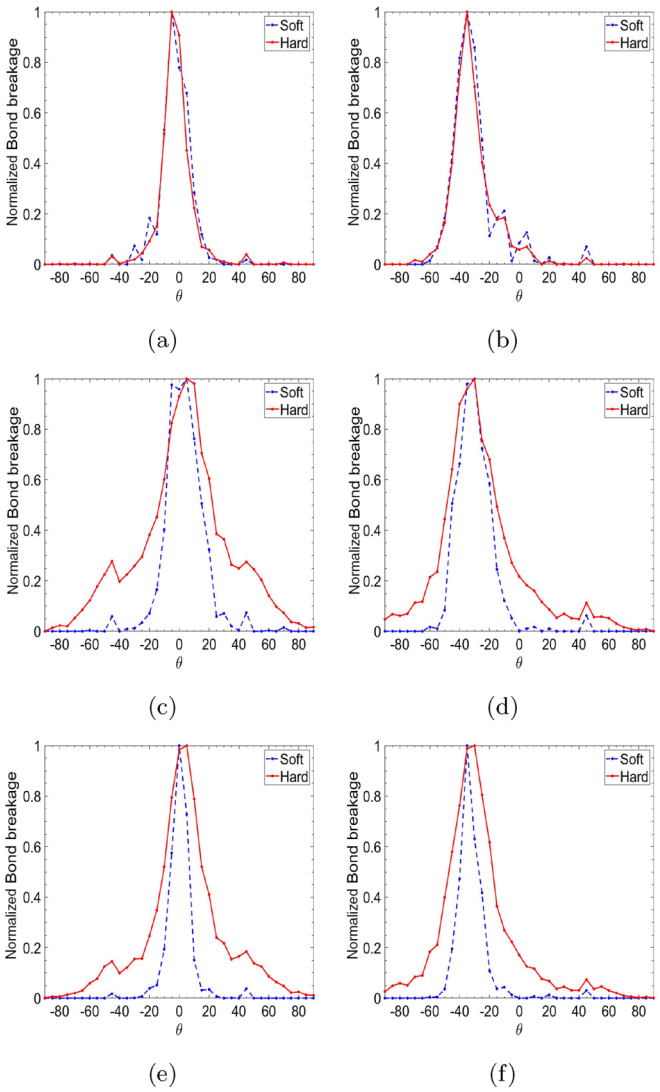

FIG. 8. For $\alpha = 20$, the angular distribution of broken hard and soft bonds, where their θ is measured about the initial crack direction in the undeformed configuration, for both mode I with (a) $r = 0.1$, (c) $r = 0.6$, and (e) $r = 0.9$ and mixed-mode loading with (b) $r = 0.1$, (d) $r = 0.6$, and (f) $r = 0.9$.

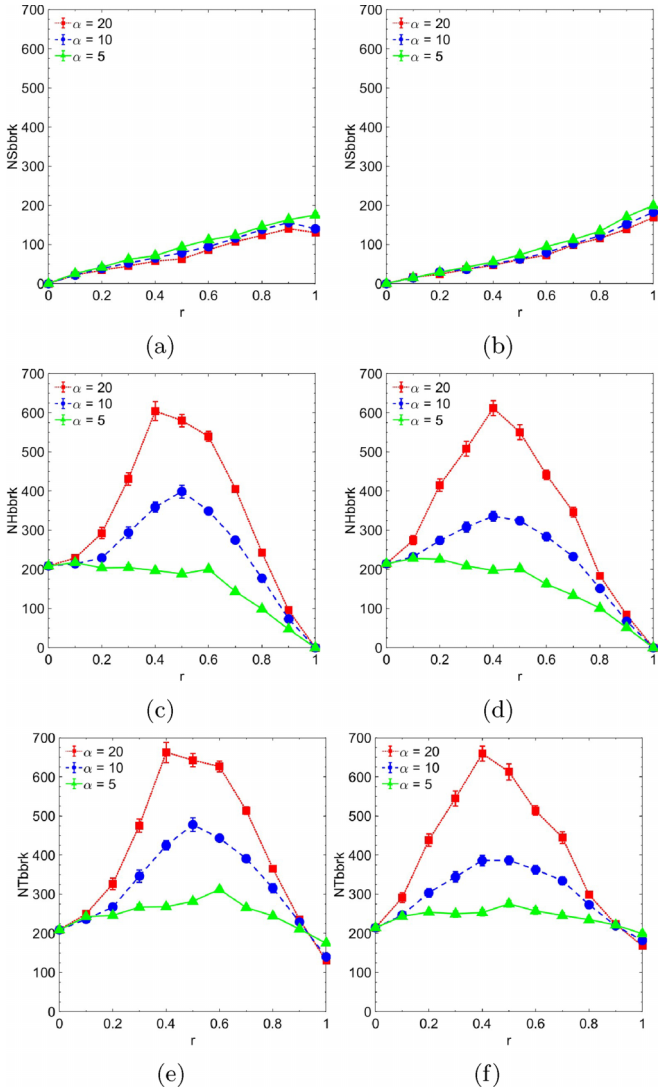

FIG. 9. In mode I loading, effect of r and α on (a) soft, (c) hard, and (e) total broken bonds and in mixed-mode loading on (b) soft, (d) hard, and (f) total broken bonds.

contributions of the two phases in the release of stored potential energy of the failed springs are presented in Fig. 10. With increasing r, the variation in the energy released closely follows the variation in number of bonds for both phases [Figs. 10(a) and 10(c)], but since the choice of failure threshold is a fixed stress, the energy released by soft bonds for higher α is higher as seen in Fig. 10(a). Comparatively, even though in the count of the number of broken bonds the hard bonds dominate Fig. 9(e), energetically, except for small r, the contribution from the softer bonds dominates the overall energy released due to breakage of bonds, as seen in Fig. 10(e). The same feature is observed for mixed mode [see Figs. 10(b), 10(d), and 10(f)]. Figure 17 in the Appendix shows the contribution of each phase in fracture energy of the system. For both fracture modes, the trend shows that beyond $r = 0.2$, the soft phase contributes more to the net fracture energy, and the contribution seems to be independent of α. With increasing r, the fraction of total energy due to breakage of hard bonds steadily decreases. For larger α the decrease is rapid initially, but for $r > 0.3$ the dissipation percentage distributes between the phases in a manner independent of α.

It is to be noted that at a higher α, the higher energy required to break soft bonds does not directly result in enhancement of strength as individually both phases ($r = 0$ and 1) have strength within 5% of each other, as seen in Figs. 4(a) and 4(b). Only when the phases are combined does the difference in the energy required to break their bonds result in more complex fracture paths and enhanced strength. In context of energy supplied to the system, however, the higher energy required to break soft bonds while expected results in higher macroscopic toughness at $r = 1$ than at $r = 0$, as seen in Figs. 4(c) and 4(d), in the range in between, i.e., $0 < r < 1$, the macroscopic toughness is higher than a linearly interpolated effective toughness, which implies there is enhancement.

Further, at $\alpha = 20$, we also simulated mode I fracture with different failure criteria by taking the energy threshold to

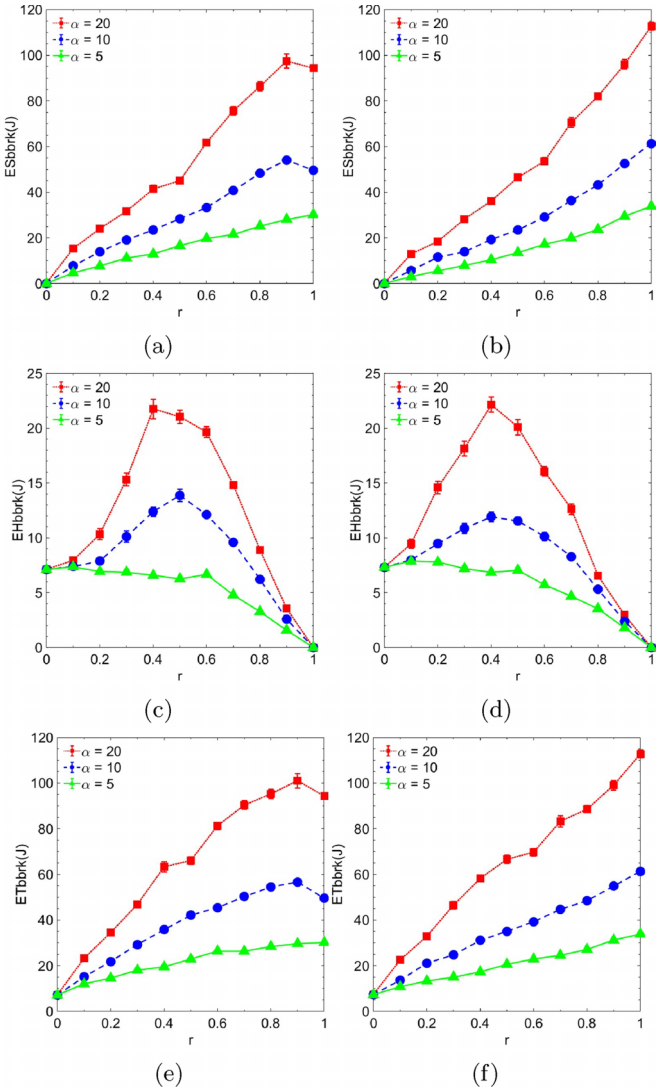

FIG. 10. In mode I loading, effect of r and α on energy dissipation due to breakage of (a) soft, (c) hard, and (e) total bonds and in mixed-mode loading on energy dissipation due to breakage of (b) soft, (d) hard, and (f) total broken bonds.

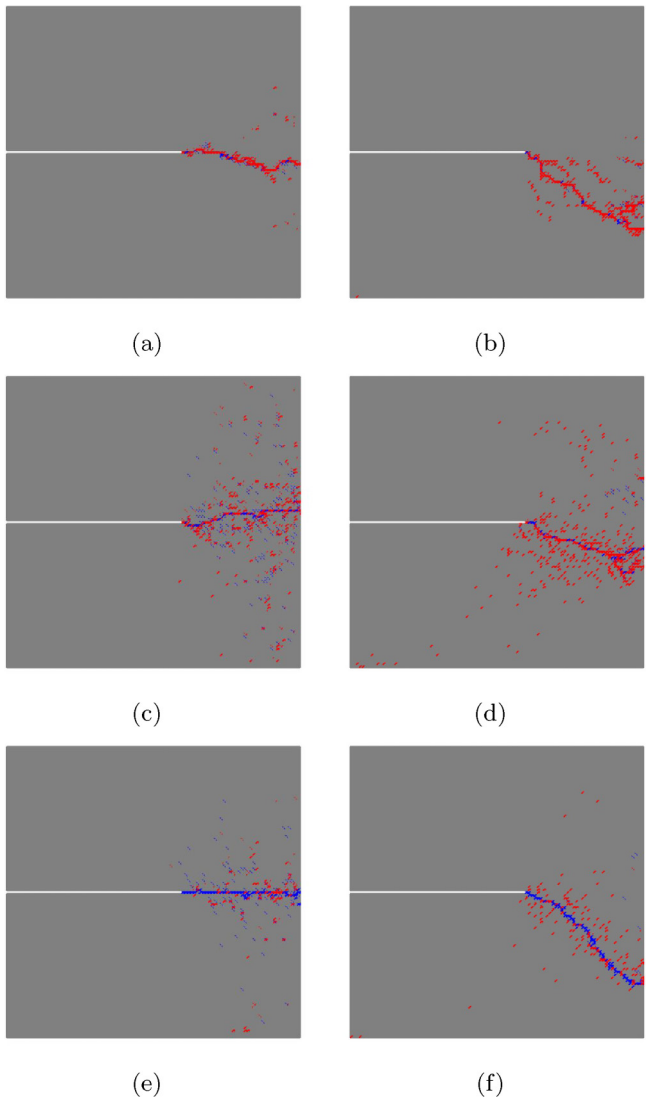

FIG. 11. Failure path of a single realization for mode I with (a) $r = 0.2$, (c) $r = 0.5$, and (e) $r = 0.8$ and for mixed mode with (b) $r = 0.2$, (d) $r = 0.5$, and (f) $r = 0.8$. Gray corresponds to unbroken bonds, blue to broken soft bonds, and red to broken hard bonds.

break the hard and soft phases as the same. We find that the strength at $r = 0.5$ is an effective average of the strength at $r = 0$ and 1 and there is no additional enhancement, while the toughness at $r = 0.5$ is slightly higher (by 4%) than the effective average. At the same energy threshold for breakage of both soft and hard phases, thus, enhancement in both strength and toughness is significantly lower. Correspondingly the crack paths at $r = 0.5$ exhibit tortuosity of 1.6 compared to 2.75 for common stress threshold criteria. This suggests that one phase being significantly more dissipative than the other as well as a fair proportion of both phases being present are vital for enhancement in strength and toughness compared to the linear interpolation between the $r = 0$ and $r = 1$ counterparts.

Regarding the optimum in EnS, seen earlier in Fig. 4(c) for mode I, it also correlates with the variations in the tortuosity. Near $r = 1$ in mode I, the tortuosity Fig. 7 sharply drops for higher α. For mixed mode, even though tortuosity is lowest at $r = 1$, it is higher than that in mode I. Lower tortuosity implies fewer bonds broken (consistent with the observation in Fig. 9 for the number of broken soft and hard bonds, respectively) and thus lower dissipation of energy at $r = 1$ for mode I.

C. Fracture type and avalanche statistics

Fracture in heterogeneous media is a competition between the two types: diffused damage growth due to heterogeneity and localized damage growth due to local stress concentrations [22]. To gain an insight into the type of damage growth for different compositions we present the crack path patterns of a single realization each in Fig. 11. Unbroken bonds are in gray, broken soft bonds are blue, and broken hard bonds are red. When the soft phase is 20% of the area, i.e., $r = 0.2$, the crack path is predominantly through the hard phase [see Fig. 11(a)], and the crack path avoids the soft phase. Even though the resulting crack path meanders around the initial

crack plane, all the broken springs are largely localized within the close neighborhood of the path. When the hard phase is 20% of the area, i.e., $r = 0.8$, as evident in Fig. 11(e), the crack path is driven primarily by the high strains ahead of the crack tip and, as any hard phase in the path is easily broken, the path does not deviate from its initial plane. However, since the soft phase has a higher strain threshold, there are quite a few soft springs, as well as hard, that break even farther from the final crack path. On the other hand, when the two phases are in equal proportion ($r = 0.5$), besides crack growth in the region of high strains ahead of the crack tip, there are a large number of damage events at multiple sites that grow independent of the crack growth. The resulting fracture process zone is very wide and has limited localization just prior to final failure as seen in Fig. 11(c). The effect of increasing r is similar when crack propagates under a remotely mixed-mode loading as seen in Figs. 11(b), 11(d), and 11(f).

The distinction between the characteristics of the two fracture types is also known to be manifested in avalanche statistics exponents [22]. Even though both fracture types exhibit scale-free power-law behavior, the heterogeneity-dominated diffused damage events, in the absence of a macroscopic crack, exhibit higher exponents (≈3.0) while the statistics of nucleation-type localized damage growth events are seen to have lower exponents (≈2.5) [22]. However, in the presence of a macroscopic crack it has been shown that even a heterogeneous solid can have lower exponents as the intensification of the stresses near the crack tip dominates, leading to localized damage growth [36].

In addition to being a signature for the type of damage growth, the study of avalanches is important in its own right as the avalanches are experimentally observable. Fracture events in heterogeneous solids are accompanied by measurable acoustic emission signals. The distribution of energy, $P_E(E)$, released in each burst of contiguous events (or avalanche), follows a power law $P_E(E) \sim E^{-\tau_E}$ [20,44–46]. In fracture simulation using the spring network model, an avalanche is defined as the number of springs that break in one increment of remotely applied strain [47–49]. We denote the probability distribution of avalanche size n by $P(n)$. The avalanche distribution is known to be a power-law distribution, $P(n) \sim n^{-\tau_n}$ for $n \gg 1$. The exponent τ_n is related to the exponent τ_E for the distribution of acoustic emission energies as $\tau_E = (1 + \tau_n)/2$. We have checked explicitly through simulations that this relation also holds for the two-phase solid for a particular choice of $\alpha = 20$ and $r = 0.4$ which has the highest total number of broken bonds. In RSNM for an elastically uniform system and in the absence of a crack, but with disordered failure threshold, numerical studies show that $\tau_n \approx 2.5$ [42].

Initially, we present the avalanche distribution for the single-phase systems of differing elastic moduli in Fig. 12. The avalanche exponent is found to be independent of the elastic moduli, as expected, and also does not appear to depend on the mode of fracture. The exponent (≈1.2) is much smaller than that reported for single-phase RSNM. However, in the presence of a macrocrack, it has been earlier observed that the value of the exponent is smaller and close to 1.2 [36].

To describe avalanches in a two-phase material, we denote the avalanches in hard and soft phases with the number of

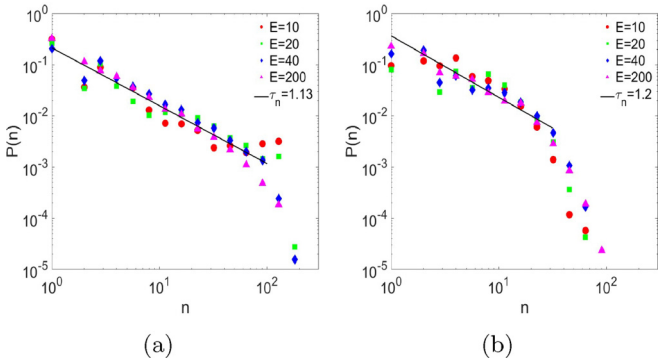

FIG. 12. The probability of an avalanche of size n, $P(n)$, in single-phase systems for different elastic moduli for (a) mode I and (b) mixed mode.

bonds broken, n_h and n_s, respectively. The complete statistics of the avalanches are then described by the joint distribution $P(n_h, n_s)$. However, given the computational constraints, it is numerically difficult to obtain good statistics for the two-dimensional avalanche distribution. Hence, we focus on the marginal distributions:

$$P_h(n_h) = \int P(n_h, n_s) dn_s, \tag{8}$$

$$P_s(n_s) = \int P(n_h, n_s) dn_h, \tag{9}$$

$$P(n) = \int P(n_h, n - n_h) dn_h, \tag{10}$$

where $P_h(n_h)$ and $P_s(n_s)$ measure the avalanche distribution for only hard and soft bonds, and $P(n)$, as defined earlier, is the avalanche distribution for the total number of bonds broken.

Examples of these distributions are shown in Fig. 13 when the composition is $r = 0.4$ for both mode I and mixed-mode loading. We find that, like for the single-phase systems, the distributions are power laws. We check that this is true for other r also. The distributions can, therefore, be characterized by exponents as follows:

$$P_h(n_h) = \frac{1}{{n_h}^{\tau_h}}. \tag{11}$$

$$P_s(n_s) = \frac{1}{{n_s}^{\tau_s}}. \tag{12}$$

$$P(n) = \frac{1}{n^{\tau_n}}. \tag{13}$$

The variation of τ_h, τ_s, and τ_n with r is summarized in Fig. 14 for $\alpha = 20$ for both modes of loading. First, we observe that the exponents depend on the composition r, and range from 1.2 to 2 with the exponent of total avalanches being maximum for $r \approx 0.5$. Second, it is evident that the power exponent of the total solid, τ_n, is closely following the one obtained for the hard phase alone, τ_h, emphasizing that the damage growth in the hard phase is the dominant

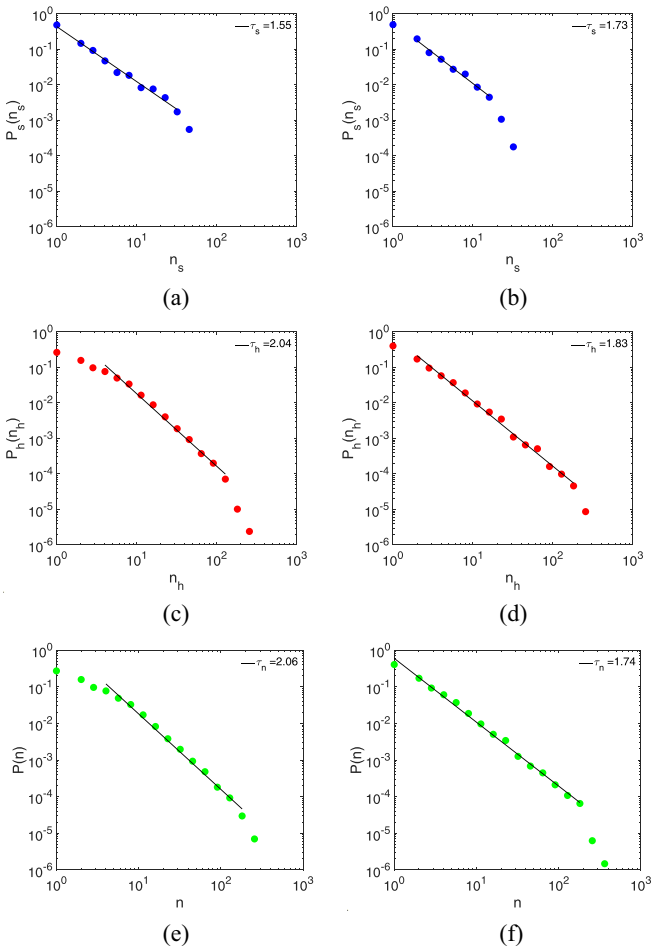

FIG. 13. For $\alpha = 20$ and $r = 0.4$, in mode I loading, the probability of an avalanche of size (a) n_s soft bonds, (c) n_h hard bonds, and (e) n total bonds and in mixed-mode loading, the probability of an avalanche of size (b) n_s soft bonds, (d) n_h hard bonds, and (f) n total bonds.

mechanism of the fracture process except at predominantly soft phase ($r \geqslant 0.8$). This observation allows us to make a few conclusions about the joint distribution of avalanches. One is

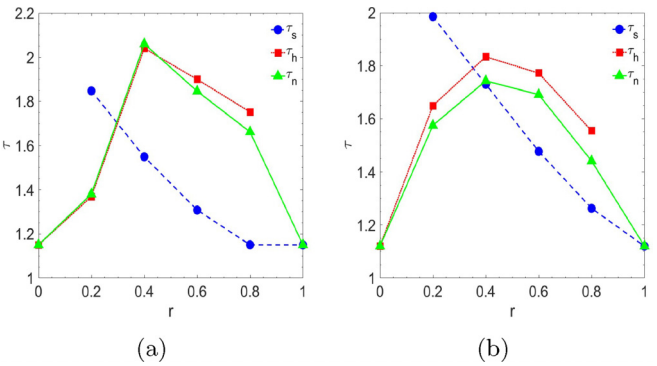

FIG. 14. The variation of τ_s, τ_h, τ_n with r for $\alpha = 20$ under (a) mode I and (b) mixed-mode loading. The distribution is separately calculated for soft, hard, and total bonds.

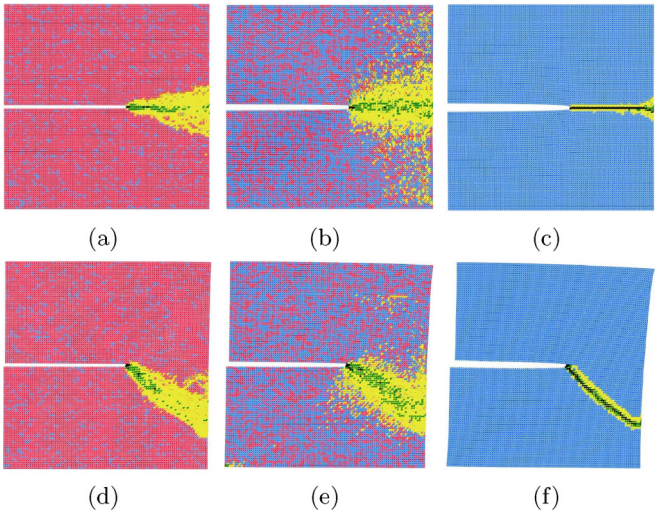

FIG. 15. Contours of failure paths averaged over 20 realizations for $\alpha = 10$ under mode I loading with (a) $r = 0.1$, (b) $r = 0.6$, and (c) $r = 1.0$ and under mixed-mode loading with (d) $r = 0.1$, (e) $r = 0.6$, and (f) $r = 1.0$. Bonds that have probability of failure in the ranges 0%–25%, 25%–50%, and greater than 50% are colored yellow, green, and black, respectively. The bonds that are not broken in any of the realizations are colored red (hard) and blue (soft), based on the composition of a single realization.

that the hard and soft avalanches are highly correlated. If this were not the case, then we could have written $P(n_h, n_s)$ in product form, $P(n_h, n_s) \approx P_h(n_h)P_s(n_s)$, and an avalanche of size n would be dominated by soft or hard bonds depending on whether $\tau_s < \tau_h$. In other words, we would obtain that $\tau_n = \min[\tau_h, \tau_s]$. This conclusion is inconsistent with our numerical results and, hence, suggests strong correlations between the breakage of hard and soft bonds.

We now connect the avalanches to the type of fracture. From Fig. 14 we observe that the exponent τ_n depends on the composition r and is largest around an evenly mixed two-phase composition ($r \approx 0.5$). This increase in avalanche exponent is related to the fracture type being avalanche type and is consistent with the diffused damage growth seen earlier in Figs. 11(c) and 11(d). At low as well as high r, the exponent τ_n is smallest, which is consistent with the damage type being nucleation dominated as observed in Figs. 11(a) and 11(e) for mode I and Figs. 11(b) and 11(f) for mixed mode.

IV. CONCLUSION

In the present work, we have used a spring network model to demonstrate that in a two-phase solid with a macroscopic crack, the enhancement in the strength of the effective response (as high as 40%) is strongly dependent on the elastic ratio between the phases when the load has mixity ($\phi = 45^\circ$ here); however, the dependence is marginal in mode I for the range of elastic ratios considered here. The enhancement is in both the strength as well as toughness, compared to the linearly interpolated between $r = 0$ and $r = 1$ counterparts. It is caused by the softer phase being significantly more dissipative than the harder phase as well as a fair proportion of both

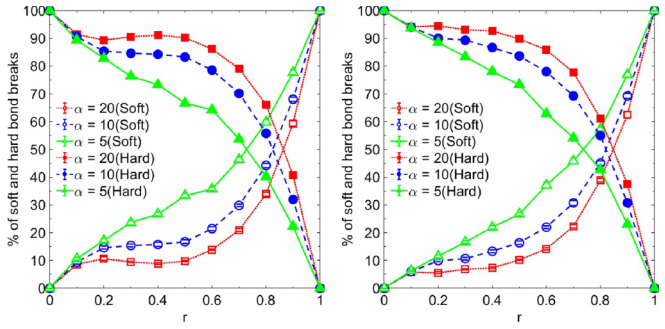

FIG. 16. Variation in percent of broken soft and hard bonds for (a) mode I and (b) mixed-mode loading with r.

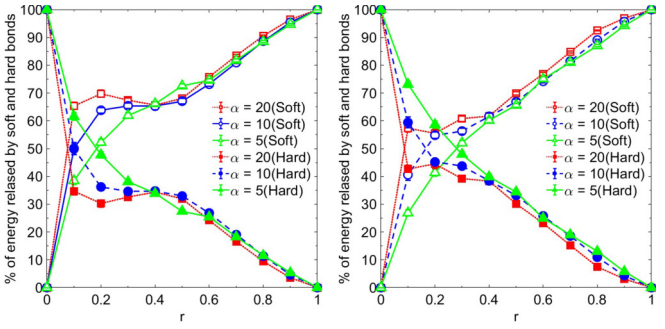

FIG. 17. Variation in percent of the total energy that is released through breakage of soft and hard bonds for (a) mode I and (b) mixed-mode loading with r.

phases being present as these result in the crack path being tortuous and its growth more dissipative.

The statistics of avalanche distribution obtained from the fracture simulations exhibit power-law behavior for both single-phase compositions as well as various ratios of two-phase compositions implying scale-free fracture behavior. The higher avalanche exponents are seen to correspond to evenly mixed phases for which avalanche-type fracture is observed. For closer to single-phase composition, whether hard or soft, the exponents are lower, and the fracture type is nucleation dominated with higher degree of localization of damage near the crack path. We also find that the avalanche exponents are different for the soft and hard phases, an aspect that would be of interest in the analysis of acoustic emission data of fracture of multiphase material.

The choice of similar breakage stress threshold used in the present study achieves a commonly observed comparative material response, that of stiffer phase being less dissipative compared to the more compliant phase. It also allows for direct evidence of strength enhancement without any further interpretations as both the limiting homogeneous cases $r = 0$ and $r = 1$ have the same strength. While the constraint of a common stress threshold would need to be modified in simulations of actual experimental data, the observed strength enhancement is expected to be qualitatively similar in a two-phase solid with a significantly tougher compliant (soft) phase.

APPENDIX

In this Appendix we give some more details of the microscopic fracture process discussed in Sec. III B.

To show the effect of α on the extent of damage, we show the fracture process zone for $\alpha = 10$ in Fig. 15. The color scheme is same as that used for Fig. 6, which is for $\alpha = 20$. It can be seen that the area of the process zone decreases with decreasing α.

Figure 16 shows the contribution of hard and soft bonds to the total number of broken bonds in both mode I and mixed mode. In Fig. 16 we see that with increasing r instead of a linear interpolation between $r = 0$ and $r = 1$, except for $r > 0.6$, the percentage of broken hard bonds dominates the overall number of broken bonds. In contrast, the energy dissipated due to breakage of bonds is dominated by the contribution from the breakage of the soft bonds, in both modes as seen in Fig. 17.

[1] J. D. Currey, Mechanical properties of mother of pearl in tension, Proc. R. Soc. London B **196**, 443 (1977).

[2] A. Jackson, J. F. Vincent, and R. Turner, The mechanical design of nacre, Proc. R. Soc. London B **234**, 415 (1988).

[3] A. Mayya, A. Banerjee, and R. Rajesh, Haversian microstructure in bovine femoral cortices: An adaptation for improved compressive strength, Mater. Sci. Eng. C **59**, 454 (2016).

[4] A. Mayya, A. Banerjee, and R. Rajesh, Role of porosity and matrix behavior on compressive fracture of Haversian bone using random spring network model, J. Mech. Behav. Biomed. Mater. **83**, 108 (2018).

[5] G. Jeronimidis, The fracture behaviour of wood and the relations between toughness and morphology, Proc. R. Soc. London B **208**, 447 (1980).

[6] T. D. Ngo, A. Kashani, G. Imbalzano, K. T. Nguyen, and D. Hui, Additive manufacturing (3D printing): A review of materials, methods, applications and challenges, Composites B: Eng. **143**, 172 (2018).

[7] R. Zou, Y. Xia, S. Liu, P. Hu, W. Hou, Q. Hu, and C. Shan, Isotropic and anisotropic elasticity and yielding of 3D printed material, Composites B: Eng. **99**, 506 (2016).

[8] D. S. Wilkinson, W. Pompe, and M. Oeschner, Modeling the mechanical behaviour of heterogeneous multi-phase materials, Prog. Mater. Sci. **46**, 379 (2001).

[9] S. Bargmann, B. Klusemann, J. Markmann, J. E. Schnabel, K. Schneider, C. Soyarslan, and J. Wilmers, Generation of 3D representative volume elements for heterogeneous materials: A review, Prog. Mater. Sci. **96**, 322 (2018).

[10] S. Yuan, S. Li, J. Zhu, and Y. Tang, Additive manufacturing of polymeric composites from material processing to structural design, Composites B: Eng. **219**, 108903 (2021).

[11] N. R. Brodnik, C.-J. Hsueh, K. T. Faber, B. Bourdin, G. Ravichandran, and K. Bhattacharya, Guiding and trapping cracks with compliant inclusions for enhancing toughness of brittle composite materials, J. Appl. Mech. **87**, 031018 (2020).

[12] L. S. Dimas, G. H. Bratzel, I. Eylon, and M. J. Buehler, Tough composites inspired by mineralized natural materials: computation, 3D printing, and testing, Adv. Funct. Mater. **23**, 4629 (2013).

[13] L. S. Dimas and M. J. Buehler, Influence of geometry on mechanical properties of bio-inspired silica-based hierarchical materials, Bioinspiration Biomimetics **7**, 036024 (2012).

[14] P. Fratzl, H. S. Gupta, F. D. Fischer, and O. Kolednik, Hindered crack propagation in materials with periodically varying Young's modulus lessons from biological materials, Adv. Mater. **19**, 2657 (2007).

[15] P. Murali, T. K. Bhandakkar, W. L. Cheah, M. H. Jhon, H. Gao, and R. Ahluwalia, Role of modulus mismatch on crack propagation and toughness enhancement in bioinspired composites, Phys. Rev. E **84**, 015102(R) (2011).

[16] S. Zapperi, A. Vespignani, and H. E. Stanley, Plasticity and avalanche behaviour in microfracturing phenomena, Nature (London) **388**, 658 (1997).

[17] L. I. Salminen, A. I. Tolvanen, and M. J. Alava, Acoustic Emission from Paper Fracture, Phys. Rev. Lett. **89**, 185503 (2002).

[18] I. Iturrioz, G. Lacidogna, and A. Carpinteri, Acoustic emission detection in concrete specimens: Experimental analysis and lattice model simulations, Intl. J. Damage Mech. **23**, 327 (2014).

[19] L. Wang, S. Cao, X. Jiang, and E. K. Salje, Cracking of human teeth: An avalanche and acoustic emission study, J. Mech. Behav. Biomed. Mater. **122**, 104666 (2021).

[20] J. Baró, P. Shyu, S. Pang, I. M. Jasiuk, E. Vives, E. K. H. Salje, and A. Planes, Avalanche criticality during compression of porcine cortical bone of different ages, Phys. Rev. E **93**, 053001 (2016).

[21] D. Boyina, T. Kirubakaran, A. Banerjee, and R. Velmurugan, Mixed-mode translaminar fracture of woven composites using a heterogeneous spring network, Mech. Mater. **91**, 64 (2015).

[22] A. Shekhawat, S. Zapperi, and J. P. Sethna, From Damage Percolation to Crack Nucleation through Finite Size Criticality, Phys. Rev. Lett. **110**, 185505 (2013).

[23] D. Kumar, A. Banerjee, and R. Rajesh, Interplay between disorder and hardening during tensile fracture of a quasi-brittle solid, Proc. R. Soc. London A **478**, 20210934 (2022).

[24] A. Mayya, P. Praveen, A. Banerjee, and R. Rajesh, Splitting fracture in bovine bone using a porosity-based spring network model, J. R. Soc. Interface **13**, 20160809 (2016).

[25] A. Mayya, A. Banerjee, and R. Rajesh, Role of matrix behavior in compressive fracture of bovine cortical bone, Phys. Rev. E **96**, 053001 (2017).

[26] W. Curtin and H. Scher, Brittle fracture in disordered materials: A spring network model, J. Mater. Res. **5**, 535 (1990).

[27] C. Urabe and S. Takesue, Fracture toughness and maximum stress in a disordered lattice system, Phys. Rev. E **82**, 016106 (2010).

[28] J. E. Bolander and N. Sukumar, Irregular lattice model for quasistatic crack propagation, Phys. Rev. B **71**, 094106 (2005).

[29] M. Yip, Z. Li, B.-S. Liao, and J. Bolander, Irregular lattice models of fracture of multiphase particulate materials, Int. J. Fract. **140**, 113 (2006).

[30] T. Wang, M. Zhou, Y. Li, Y. Yu, and H. He, Lattice spring model with angle spring and its application in fracture simulation of elastic brittle materials, Theor. Appl. Fract. Mech. **106**, 102469 (2020).

[31] B. Sun, X. Huang, Y. Zheng, and L. Guo, Multi-scale lattice method for mesoscopic crack growth simulation of concrete structures, Theor. Appl. Fract. Mech. **106**, 102475 (2020).

[32] J. Liu, S. Deng, J. Zhang, and N. Liang, Lattice type of fracture model for concrete, Theor. Appl. Fract. Mech. **48**, 269 (2007).

[33] L. Brely, F. Bosia, and N. M. Pugno, A hierarchical lattice spring model to simulate the mechanics of 2-D materials-based composites, Front. Mater. **2**, 51 (2015).

[34] L. S. Dimas, T. Giesa, and M. J. Buehler, Coupled continuum and discrete analysis of random heterogeneous materials: Elasticity and fracture, J. Mech. Phys. Solids **63**, 481 (2014).

[35] L. S. Dimas, D. Veneziano, T. Giesa, and M. J. Buehler, Random bulk properties of heterogeneous rectangular blocks with lognormal Young's modulus: Effective moduli, J. Appl. Mech. **82**, 011003 (2015).

[36] R. P. S. Parihar, D. V. Mani, A. Banerjee, and R. Rajesh, Role of spatial patterns in fracture of disordered multiphase materials, Phys. Rev. E **102**, 053002 (2020).

[37] D. Kumar, A. Banerjee, and R. Rajesh, Crushing of square honeycombs using disordered spring network model, Mech. Mater. **160**, 103947 (2021).

[38] M. Aliha, H. Ziari, B. Mojaradi, and M. J. Sarbijan, Heterogeneity effects on mixed-mode I/II stress intensity factors and fracture path of laboratory asphalt mixtures in the shape of SCB specimen, Fatigue Fract. Eng. Mater. Struct. **43**, 586 (2020).

[39] Y. Chen, A. Eskandarian, M. Oskard, and J. Lee, Meshless simulation of crack propagation in multiphase materials, Theor. Appl. Fract. Mech. **45**, 13 (2006).

[40] E. Torabi, S. Ghouli, L. Maravina, and M. R. Ayatollahi, Mixed mode fracture behavior of short-particle engineered wood, Theor. Appl. Fract. Mech. **115**, 103054 (2021).

[41] L. Monette and M. Anderson, Elastic and fracture properties of the two-dimensional triangular and square lattices, Modell. Simul. Mater. Sci. Eng. **2**, 53 (1994).

[42] M. J. Alava, P. K. Nukala, and S. Zapperi, Statistical models of fracture, Adv. Phys. **55**, 349 (2006).

[43] S. Senapati, A. Banerjee, and R. Rajesh, Simulation of mixed-mode fracture in a single phase and two-phase composite material, in *Recent Advances in Applied Mechanics*, edited by T. Tadepalli and V. Narayanamurthy (Springer, Singapore, 2022), pp. 247–260.

[44] E. K. Salje, X. Jiang, J. Eckstein, and L. Wang, Acoustic emission spectroscopy: Applications in geomaterials and related materials, Appl. Sci. **11**, 8801 (2021).

[45] A. Petri, G. Paparo, A. Vespignani, A. Alippi, and M. Costantini, Experimental Evidence for Critical Dynamics in Microfracturing Processes, Phys. Rev. Lett. **73**, 3423 (1994).

[46] A. Guarino, S. Ciliberto, A. Garcimartın, M. Zei, and R. Scorretti, Failure time and critical behaviour of fracture precursors in heterogeneous materials, Eur. Phys. J. B **26**, 141 (2002).

[47] P. C. Hemmer and A. Hansen, The distribution of simultaneous fiber failures in fiber bundles, J. Appl. Mech. **59**, 909 (1992).

[48] S. Zapperi, P. Ray, H. E. Stanley, and A. Vespignani, Avalanches in breakdown and fracture processes, Phys. Rev. E **59**, 5049 (1999).

[49] J. T. Kjellstadli, Burst distribution by asymptotic expansion in the equal load sharing fiber bundle model, Front. Phys. **7**, 201 (2019).